Silicon Photonics Rectangular Universal Interferometer

Daniel Perez, Ivana Gasulla, Francisco Javier Fraile, Lee Crudgington, David J. Thomson, Ali Z. Khokhar, Ke Li, Wei Cao, Goran Z. Mashanovich, and Jose Capmany*

Universal multiport photonic interferometers that can implement any arbitrary unitary transformation between input and output optical modes are essential to support advanced optical functions. Integrated versions of these components can be implemented by means of either a fixed triangular or a fixed rectangular arrangement of the same components. We propose the implementation of a fixed rectangular universal interferometer using a reconfigurable hexagonal waveguide mesh circuit. A suitable adaptation synthesis algorithm tailored to this mesh configuration is provided and the experimental demonstration of a rectangular multiport interferometer by means of a fabricated silicon photonics chip is reported. The 7-hexagonal cell chip can implement 2 × 2, 3 × 3 and 4 × 4 arbitrary unitary transformations. The proposed hexagonal waveguide mesh operates in a similar way as a Field Programmable Gate Array (FPGA) in electronics. We believe that this work represents an important step-forward towards fully programmable and integrable multiport interferometers.

1. Introduction

Universal multiport photonic interferometers based on planar arrangements of reconfigurable beam splitting and phase shifting devices can implement any arbitrary unitary transformation between input and output optical modes.[1,2] These arbitrary transformations are essential to support advanced optical functions, which include, among others, linear quantum optical gates and circuits[3–5] microwave photonics signal processors,[6] spatial mode converters,[7,8] data center connections[9] and optical networking functionalities.[10]

D. Perez, Dr. I. Gasulla, Prof. J. Capmany
ITEAM Research Institute
Universitat Politècnica de València
Valencia, 46022, Spain
E-mail: jcapmany@iteam.upv.es

Prof. F. J. Fraile
Dept. Teoría de la Señal y Comunicaciones
Universidad de Vigo
ETSI Telecomunicación
Vigo, 36310, Spain

Dr. L. Crudgington, Dr. D. J. Thomson, Dr. A. Z. Khokhar, Dr. K. Li, Dr. W. Cao, Prof. G. Z. Mashanovich
Optoelectronics Research Centre
University of Southampton
Hampshire, Southampton, SO17 1BJ, United Kingdom

The most common design for universal photonic interferometers is based on the triangular arrangement of ideal 2 × 2 beam splitters and phase shifters proposed by Reck et al.[1] and extended to feature the possibility of self-reconfiguration and the use of non-ideal components by Miller.[11] Very recently, however, Clements et al.[12] have proposed a new design, which is based on a rectangular arrangement of 2 × 2 beam splitters and phase shifters and requires half the optical depth as compared to the triangular arrangement. This feature makes this design more robust against losses and fabrication errors.

The planar waveguide arrangement lends itself to easy chip integration in a silicon photonics platform, where the reconfigurable beam splitters can be implemented by means of Mach-Zehnder interferometers (MZIs),[11] while self-configuration, programming and error monitoring can be implemented using auxiliary transparent detectors[2] and/or CMOS compatible contactless integrated photonic probes (CLIPPs).[13]

Several experimental demonstrations of the triangular arrangement have been reported very recently,[8,14] but there is still, to our knowledge, no experimental results reported for the rectangular arrangement. One possibility for its compact implementation is to employ a hardware architecture that follows the design principles similar to those of the Field Programmable Gate Arrays (FPGAs) in electronics.[15] The core concept is to use a large network of identical two-dimensional (2D) unit or lattice cells implemented by means of MZI waveguides, as proposed by Zhuang and co-workers.[16] With a proper MZI waveguide lattice design, this architecture is capable of implementing different interferometric filtering (i. e. Mach-Zehnder, transversal and optical ring cavity) configurations by mapping the desired unitary matrix implementation to a selection of adequate signal paths through the mesh and using a synthesis algorithm that translates the routing requirements into independent tuning of circuit parameters. In particular, by introducing phase tuning elements in both arms of the MZI waveguides in the grid to enable independent control of amplitude and phase of light. Furthermore, although this was not proposed in,[16] a MZI waveguide mesh can also be employed to implement multiple input/multiple output linear unitary transformations.

While Zhuang and co-workers proposed a square waveguide mesh, we recently demonstrated that a hexagonal lattice features improved performance in terms of spatial tuning reconfiguration

ADVANCED
SCIENCE NEWS

www.advancedsciencenews.com

LASER
&PHOTONICS
REVIEWS

www.lpr-journal.org

step, reconfiguration performance, switching elements per unit area, and losses per spatial resolution.[17] We thus propose the use of the hexagonal waveguide mesh topology to implement multiple input/multiple output rectangular universal interferometer. Here we show and experimentally demonstrate that the hexagonal waveguide lattice enables a simple implementation of the rectangular universal multiport interferometer proposed in.[12] We first briefly review the concept of hexagonal waveguide mesh outlining its relevant design parameters. We then show how this mesh architecture can implement the rectangular universal interferometer arrangement and provide the adaptation of the synthesis algorithm proposed in[12] including some design examples. We subsequently report the fabrication and experimental demonstration of a rectangular multiport interferometer based on a 7-cell silicon photonics hexagonal waveguide mesh. Linear 2 × 2, 3 × 3 and 4 × 4 matrix transformations are shown. Finally, we discuss the limitations related to the scalability of the mesh (i. e., number of input/output ports), internal losses, non-ideal values of the required tuning elements and side thermal effects.

2. Background

The proposed MZI waveguide mesh topology for the multiport interferometer is shown in **Figure 1**a (in this particular case a 12 input/12 output port configuration). Figure 1b shows a limited region corresponding to 7 cells that actually corresponds to the fabricated device,.[17] Each lattice or 2D unit cell is a hexagon, where each one of its six sides, also known as basic unit length (BUL), is composed of two close waveguides. These waveguides are connected, as shown in Figure 1c, by means of a tunable basic unit (TBU) composed of 2 3-dB couplers and 2 parallel waveguides loaded with phase shifters, ϕ_{upper} and ϕ_{lower}, respectively. This MZI performs a coupler with independent amplitude and phase shifting capabilities and its ideal transfer matrix is given by:

$$h_{TBU} = je^{j\Delta} \begin{pmatrix} \sin\theta & \cos\theta \\ \cos\theta & -\sin\theta \end{pmatrix}, \tag{1}$$

where θ is $(\phi_{upper} - \phi_{lower})/2$ and Δ is $(\phi_{upper} + \phi_{lower})/2$.

By means of external electronic control signals applied to the heaters deposited on top of each MZI arm, each TBU can be configured to provide independent power splitting ratio and overall phase shift. This ability enables the operation as a directional coupler or simply as an optical switch in a cross or bar state (as shown in Figure 1c) providing amplitude- and phase-controlled optical routing.[2,16] Using this principle, this waveguide mesh architecture can be reconfigured to support different connection paths between its input and output ports and, hence, any kind of linear transformation, much in the same way as a FPGA operates in electronics.

3. Interferometer Implementation

Figure 2a and b display an example illustrating the implementation of a 9 × 9 multiport interferometer based on the rectangular arrangement proposed by Clements et al.[12]

To adapt this layout and its synthesis algorithm to the hexagonal waveguide mesh, we need to perform a few modifications. First of all, we must use a different matrix for the beam coupler/ TBU structure. In our case, as can be seen in Figure 2c and d, we employ a TBU for the tunable coupler (colored in green), defined by a transfer function h_{TC}, and the 2 precedent TBUs (colored in black) for the required connections. Here, the upper one operates in cross mode providing an extra phase shifting (Upper Phase Shifter, h_{TC}), while the lower one operates in cross mode.

Since these 2 TBUs are set in cross state, we can write the transfer matrix of the full beam coupler as:

$$h_{BC} = -e^{j\Delta} \begin{pmatrix} e^{j\phi}\sin\theta & \cos\theta \\ e^{i\phi}\cos\theta & -\sin\theta \end{pmatrix} =$$
$$= -\begin{pmatrix} e^{j\phi}r & t \\ e^{i\phi}t & -r \end{pmatrix}. \tag{2}$$

The algorithm proceeds by nulling successive matrix elements starting from the targeted unitary (N x N) matrix U. Depending on the location of the element U(n,m) to be cancelled, a row or column combination of the matrix is required.

If *N-n-m* is odd, then, the element to be nulled requires a combination of columns n and m, and the updating process is done by the following transformation:

$$U^{Upd} = UT_{n,m}^{-1}. \tag{3}$$

While if *N-n-m* is even, then, the element to be nulled requires a combination of rows n and m, and the updating process is done by the following transformation:

$$U^{Upd} = T_{n,m}U, \tag{4}$$

where, for the case of the hexagonal waveguide mesh:

$$T_{m,n} = \begin{bmatrix} 1 & 0 & \cdots & \cdots & \cdots & \cdots & \cdots & 0 \\ 0 & 1 & & & & & & \\ \cdot & & \cdot & & & & & \\ \cdot & & & e^{i\phi}r & t & & & \\ \cdot & & & e^{i\phi}t & -r & & & \\ \cdot & & & & & \cdot & & \\ \cdot & & & & & & 1 & 0 \\ 0 & \cdots & \cdots & \cdots & \cdots & \cdots & 0 & 1 \end{bmatrix}. \tag{5}$$

By further developing Equations (3) and (4), we can obtain an equation that relates the value of the matrix element U(n,m) to be nulled with the t and ϕ values of the corresponding T-matrix. For odd parity *(N-n-m)* (i. e., the matrix U(n,m) sub-diagonals nulled in the 1st, 3rd, 5th, 7th place, etc.), we have:

$$|t| = \sqrt{\frac{|U(n,m)|^2}{|U(n,m)|^2 + |U(n,m+1)|^2}},$$
$$\phi = \angle U(n,m) - \angle U(n,m+1) - \pi, \tag{6}$$

while for even parity *(N-n-m)* elements (i. e., the matrix U(n,m) sub-diagonals nulled in the 2nd, 4th, 6th, 8th place, etc.), we
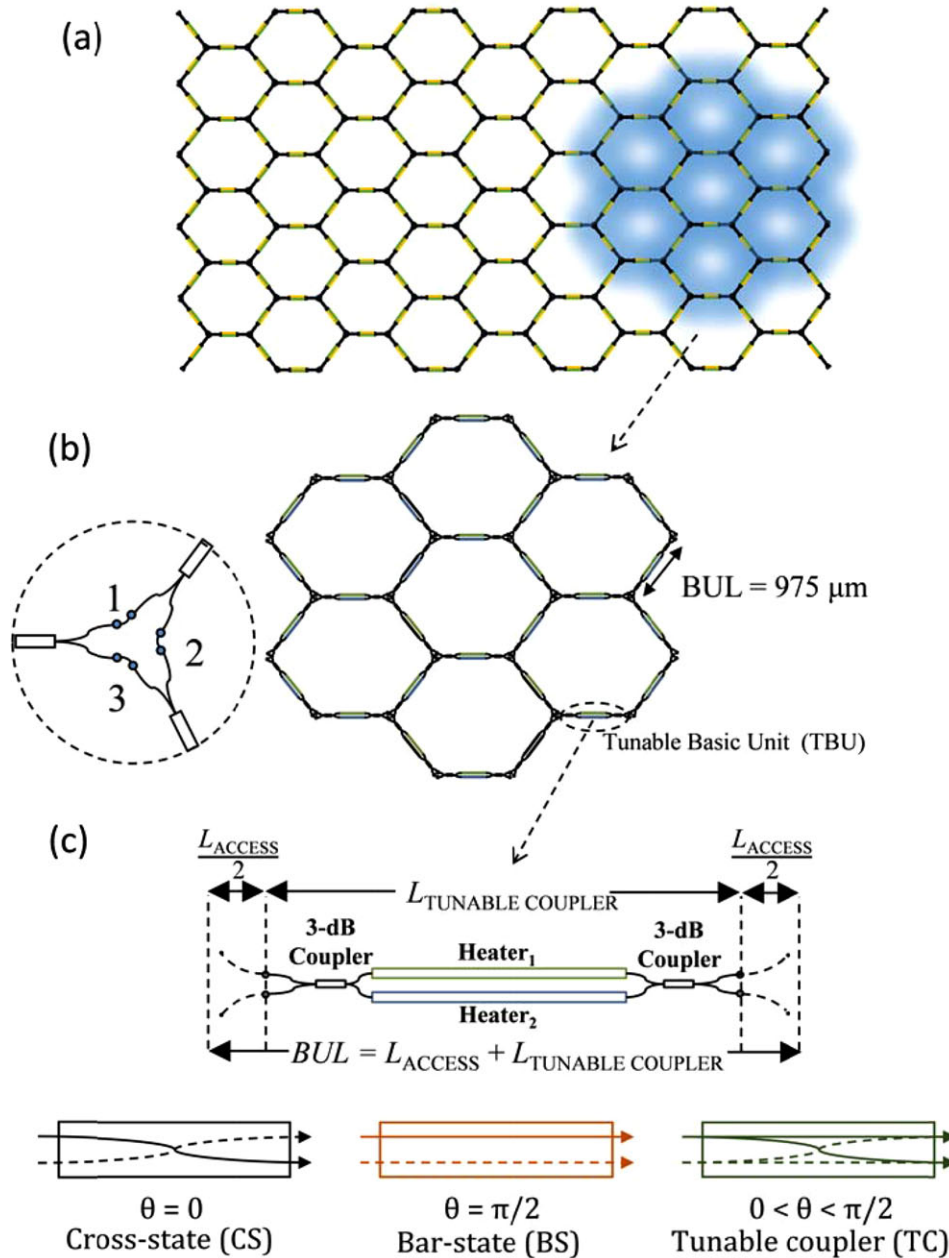
Figure 1. a) Generic layout of the proposed hexagonal waveguide mesh. b) A 7-hexagonal cell layout that corresponds to the fabricated device. c) Detailed configuration of the side of a hexagon lattice or Basic unit length (BUL) that comprises the access segments (input and output) and the internal tunable basic unit (TBU) implemented by means of a Mach-Zehnder Interferometer (MZI) closed by two Multimode Interference (MMI) 3-dB couplers.

have:

$$|t| = \sqrt{\frac{|U(n, m)|^2}{|U(n, m)|^2 + |U(n-1, m)|^2}}, \quad (7)$$

$$\phi = \angle U(n, m) - \angle U(n-1, m).$$

To complete the algorithm, we must also consider the special case where the element to be nulled is a priori 0. In this case, t must be set to 0 to prevent a mathematical error. When the algorithm has finished, the resulting U will be a diagonal matrix of

unit amplitude (i. e. phase-only) elements. For a given equivalent beam splitter in the hexagonal mesh, the resulting t and phase shift ϕ values are transformed into the following values for its internal phase shifters:

$$\phi_{TCupper} = \theta = \arccos(|t|),$$

$$\phi_{TClower} = -\theta,$$

$$\phi_{LPSupper} = \phi_{LPSlower} = 0, \quad (8)$$
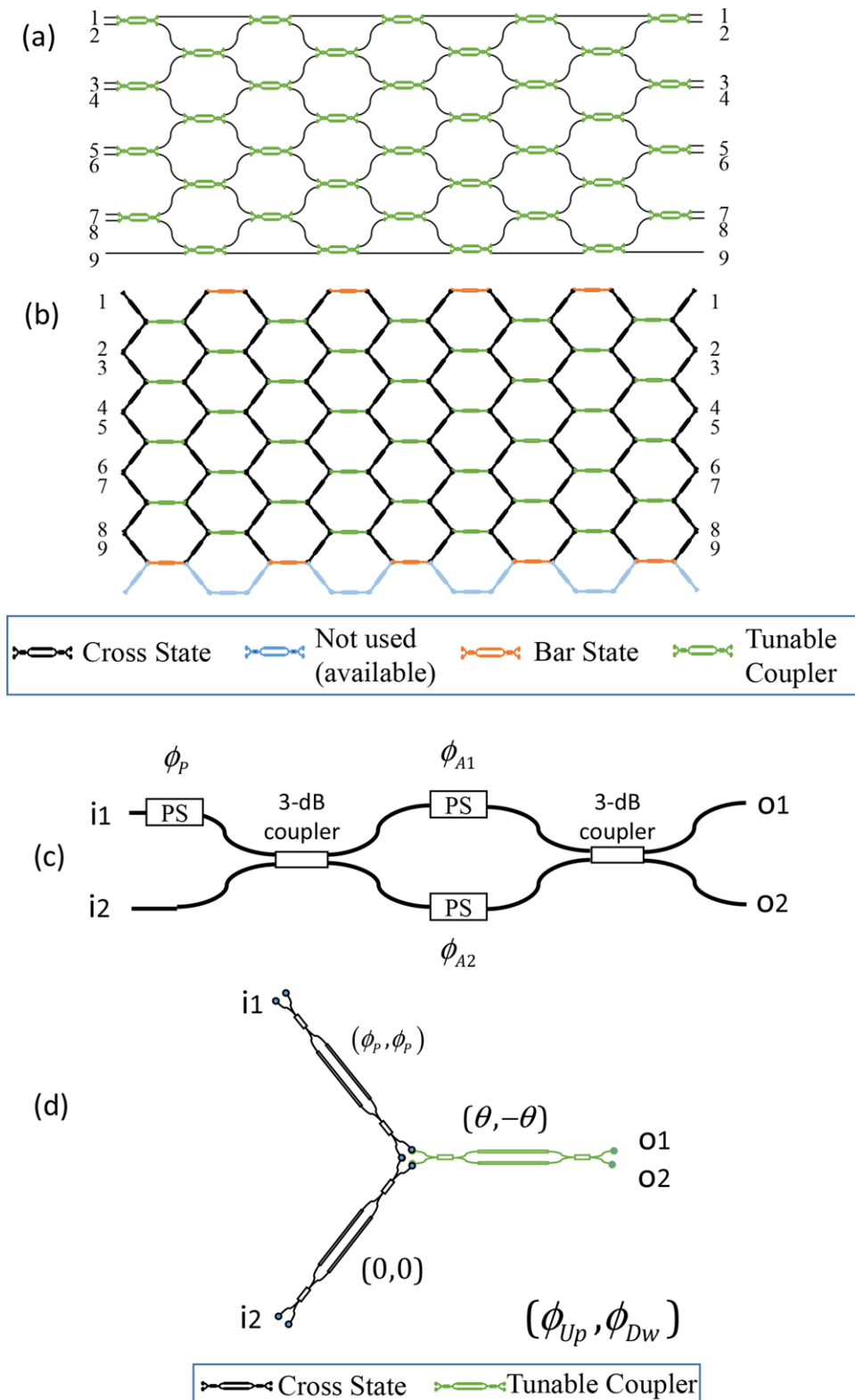
1700219 (3 of 13)

Figure 2. a) Rectangular arrangement of a 9 × 9 interferometer as proposed in.[12] b) Equivalent implementation using the hexagonal waveguide mesh proposed in this paper. c) MZI and phase shifter arrangement proposed in[12] for the implementation of the beam splitters in the rectangular arrangement. d) Equivalent configuration for the MZI and phase shifter arrangement using the elements available in the hexagonal cell. (ϕ_{up}, ϕ_{dw}) are the upper and lower phase shift applied to each TBU arm).
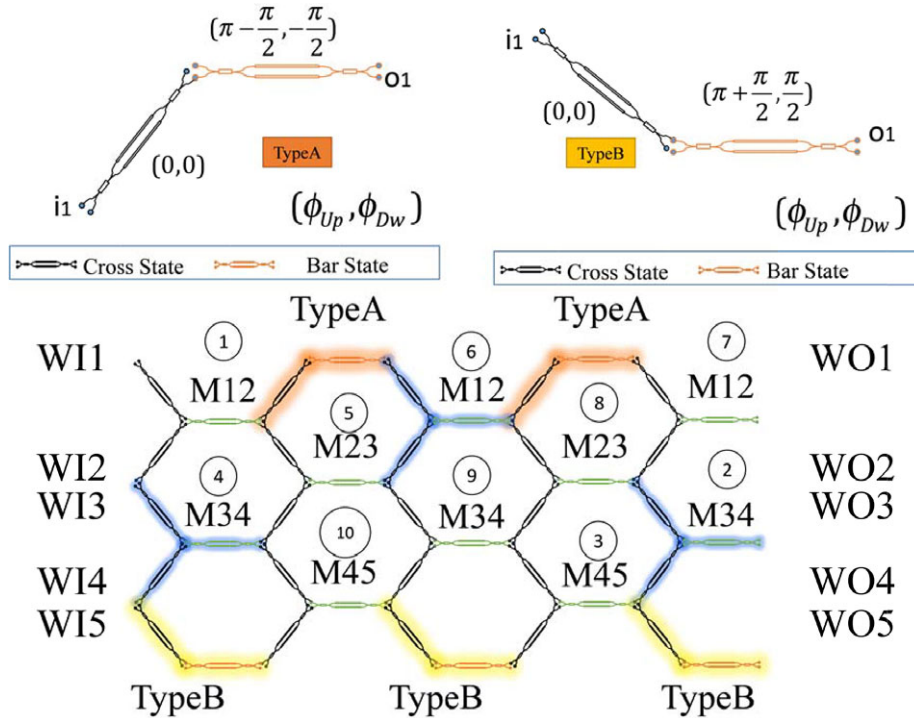
Figure 3. Rectangular arrangement of a 5 × 5 interferometer showing the outer path configurations (up), and their location within the mesh configuration (bottom). The order of the settings followed by the synthesis algorithm are indicated. WI: Input Waveguide, WO: Output Waveguide; MXY: Coupler with amplitude and phase tuning capabilities (in green).

$$\phi_{UPSupper} = \phi_{UPSlower} = \phi,$$

$$[\phi_{io1} \ldots \phi_{ioN}] = diag(U^{lastupdated}) - \frac{\pi}{2},$$

where ϕ_{ion} are the phase shifts on all individual channels at the output of the interferometer that compensate for complex values on the diagonal matrix U at the last updating step.

Finally, some of the outer TBUs that build up the interferometer must be configured to be phase-transparent featuring the phase-shift values indicated in the upper part of **Figure 3** for both possible configurations, labelled as Type A and Type B, respectively.

A procedure describing the synthesis algorithm is the following:

```
1:   procedure Programme (U)
2:       for i from 1 to N-1 do
3:           if i is odd then
4:               for j = 0 to i-1 do
5:                   if U (N-j, i-j) is 0 then
6:                       t = 0;
7:                   else
8:                       %null U(N-j, i-j) by T⁻¹_{i-j, i-j+1} Eq.(6)
```

```
9:                       %update U T⁻¹_{i-j, i-j+1}
10:          else
11:              for j = 1 to i do
12:                  if U (N+j-i,j) is 0 then
13:                      t = 0;
14:                  else
15:                      %null U(N+j-i,j) by T_{N+j-i-1, N+j-i} Eq.(7)
16:                      %update T_{N+j-i-1, N+j-i} U
17:          % compute Δ,φ, θ Equation (8)
```

In order to illustrate the procedure, we have chosen two application examples. The first one represents the linear transformation corresponding to a three-way beamsplitter given by the unitary matrix:[2]

$$U_{tritter} = \frac{1}{\sqrt{3}} \begin{pmatrix} 1 & 1 & 1 \\ 1 & e^{i2\pi/3} & e^{i4\pi/3} \\ 1 & e^{i4\pi/3} & e^{i8\pi/3} \end{pmatrix}. \tag{9}$$

To synthesize the linear transformation given by Equation (9), the procedure described above for the rectangular arrangement yields the structure indicated in **Figure 4**, where the labelled configuration for each TBU is depicted, specifying: ID, for the TBU identification label, K, for the coupling constant, ϕ for the
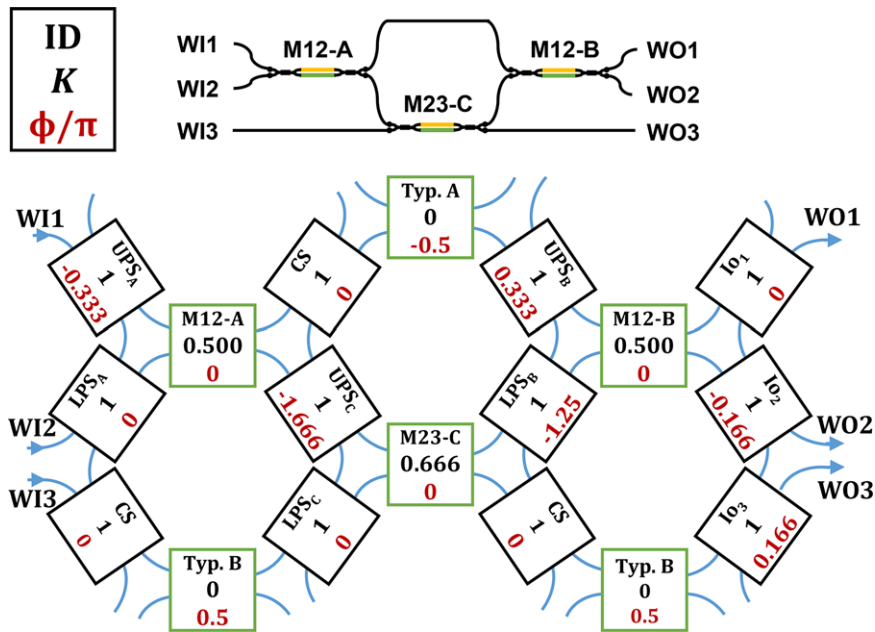
Figure 4. Layout of the implementation of the three-way beamsplitter using a 3 × 3 interferometer with rectangular beam splitter arrangement (Upper). Actual implementation of the 3 × 3 interferometer using a hexagonal-mesh with the labeled configuration for each Tunable Basic Unit (TBU) (lower). ID: TBU identification label where MXY-Z identifies the coupler with amplitude and phase tuning capabilities (in green) and Z the letter that brings the order of being solved by the algorithm, K: coupling constant, ϕ: additional phase shift.
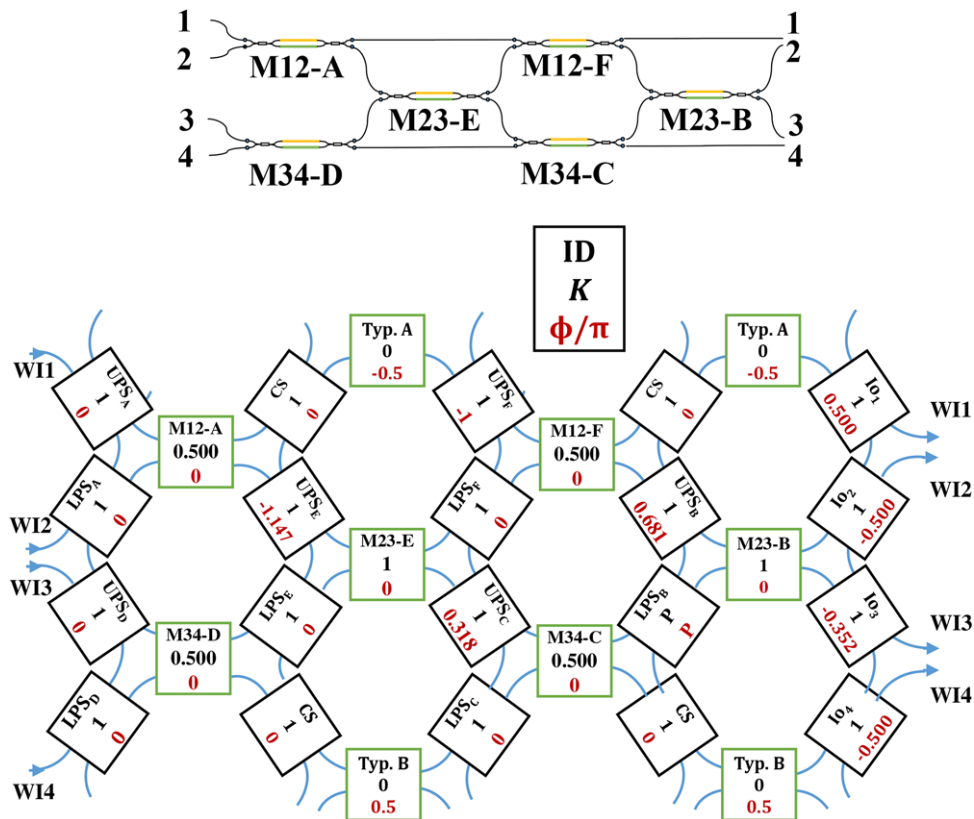

Figure 5. Layout of the implementation of the Hadamard transformation using a 4 × 4 interferometer with rectangular beam splitter arrangement (Upper). Actual implementation of the 4 × 4 interferometer using a hexagonal-mesh with the labeled configuration for each Tunable Basic Unit (TBU) (lower). ID: TBU identification label where MXY-Z identifies the coupler with amplitude and phase tuning capabilities (in green) and Z the letter that brings the order of being solved by the algorithm, K: coupling constant, ϕ: additional phase shift.

ADVANCED
SCIENCE NEWS
www.advancedsciencenews.com

LASER
& PHOTONICS
REVIEWS

www.lpr-journal.org

additional phase shift. The detailed derivation and explanation is provided in the Supporting Information.

The second example corresponds to a 4 × 4 Hadamard transformation given by:

$$U_{Hadamard} = \frac{1}{\sqrt{2^2}} \begin{pmatrix} 1 & 1 & 1 & 1 \\ 1 & -1 & 1 & -1 \\ 1 & 1 & -1 & -1 \\ 1 & -1 & -1 & 1 \end{pmatrix}. \qquad (10)$$

The synthesis procedure yields in this case the layout depicted in **Figure 5**.

4. Chip Fabrication, Characterization and Operation

4.1. Fabrication

A waveguide mesh consisting of 7 hexagonal cells was fabricated at the Southampton Nanofabrication Centre at the University of Southampton. Silicon on insulator (SOI) wafers with a 220-nm thick silicon over-layer and a 3-μm thick buried oxide layer were used and e-beam lithography performed to define the grating couplers. Dry etching of 70 nm into the silicon over-layer to form the grating couplers was then carried out followed by resist stripping.

Another e-beam lithography and 120-nm silicon dry etching step was performed to produce the optical waveguides. Following resist stripping, 1 μm of PECVD silicon dioxide was deposited to act as the upper cladding layer of the waveguides. Photolithography was then performed to define isolation trench openings, followed by a deep dry etching process to etch through the top cladding, silicon over-layer and buried oxide layer. These trenches provided thermal isolation to adjacent devices and improved the efficiency of the heaters. A 1.8-μm thick metal layer was deposited after the resist had been stripped. A subsequent photolithography and dry etching step realized electrodes used to provide localized heating to tune the devices. The resist was then stripped and the wafers diced into individual dies. These dies were then mounted onto PCBs and a wire bonding process was used to provide electrical connections both within the die and between the die and the PCB.

Figure 6a shows the fabricated chip that occupies a surface of 15 × 20 mm^2, includes 30 MZIs, 60 thermal tuners and 120 pads, and features 24 optical input/output ports mounted on a printed circuit board (PCB) that occupies a surface of 60 × 120. Multimode interference (MMI) couplers rather than directional couplers were employed for the implementation of the MZI 3-dB power splitters as they were already optimized in previous internal fabrication rounds. The use of MMIs sacrifices device footprint in order to offer a wideband response with insertion losses lower than 0.2 dB and 3-dB splitting ratios better than 3%. The test structure shown in the left hand-side has an additional 8 MZIs (6 + 2), 16 thermal tuners and 32 pads. The inset shows the top-view of the 7-cell mesh with the wire-bonding for the electrical feeding. Figure 6b display a zoom view of the 7-hexagonal mesh (hexagon BUL is 975 μm) mm^2.
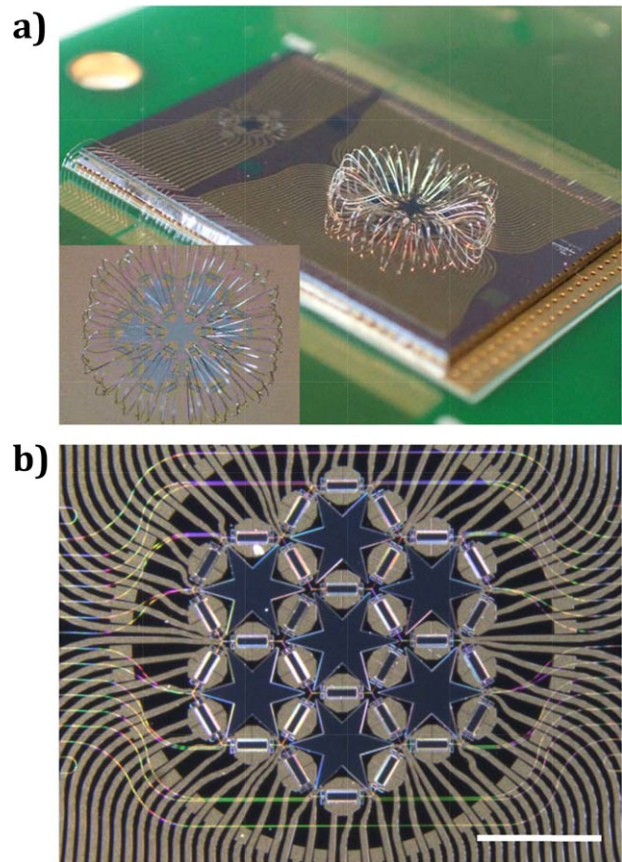

Figure 6. a) 15 × 20 mm^2 chip mounted on a printed circuit board (PCB) of footprint 120 × 60 mm^2 and (inset) top-view of the wire-bondings. b) Zoomed view of the fabricated 7-hexagonal mesh. The scale bar is equivalent to 2 mm.

4.2. Characterization and Operation

We carried a static characterization of the test cell in four different dies to extract information regarding the main optical properties of the integrated waveguides. **Figure 7**a shows the diagram corresponding to the test setup, while Figure 7b displays the actual configuration assembled in the laboratory. This configuration was also employed to obtain the experimental results reported in the next section. The full static testing of the device included propagation, bend and insertion losses as well as thermal stability using the test cell. We measured the spectral region of operation for the input/output grating coupler devices and found that the optimum performance was in the 1580 ± 15 nm range rather than the targeted 1550 nm. We obtained full calibration curves for the coupling constants and phase shift versus injected current for all the 30 MZIs in the structure, as well as a detailed characterization of the thermal crosstalk.

A tunable laser (ANDO AQ4321D) featuring a 1-pm wavelength resolution was connected to the input grating coupler of the test cell and scanned to provide a wavelength range characterization. The test cell output grating coupler was connected to an optical spectrum analyzer (ANDO AQ6217C). The performed measurements included: differential path length to character-
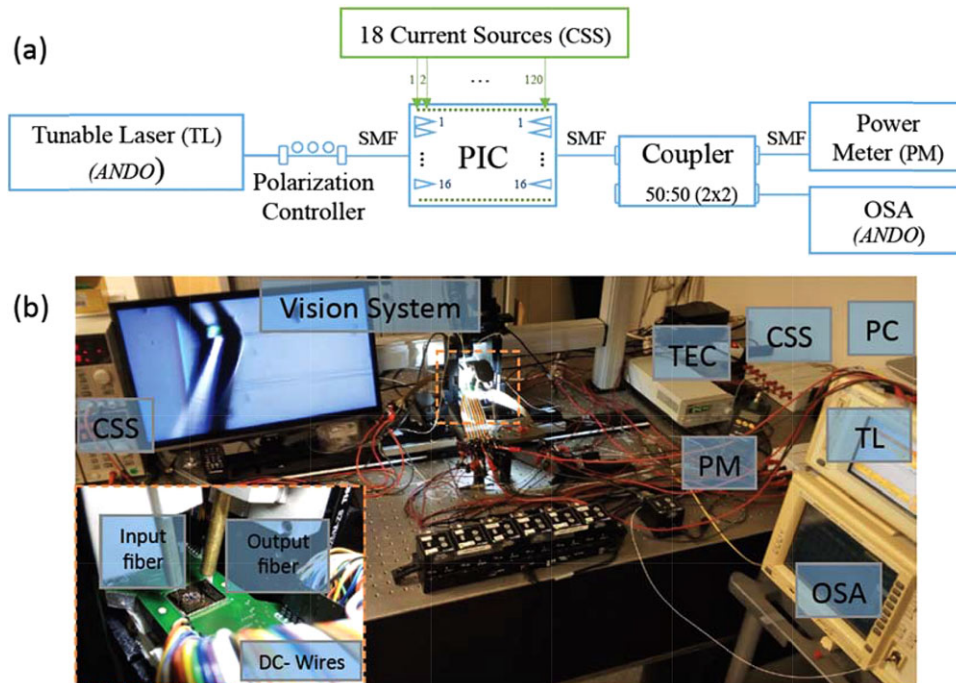
**ADVANCED
SCIENCE NEWS**

www.advancedsciencenews.com

LASER
&PHOTONICS
REVIEWS

www.lpr-journal.org

Figure 7. a) Diagram for the testing setup employed to characterize the fabricated chip including a separate test structure. b) Setup implementation in the laboratory. The zoomed part corresponds to the location of the chip, including the input and output fiber assemblies.

ize propagation losses, cascaded bends structures to characterize bend losses and 2 different cascaded and coupled MMI structures to characterize MMI insertion losses and bandwidth. For electro-optical characterization of the TBUs in the 7-cell waveguide mesh, we employed 18 current sources of different resolution and quality: 3 Keihtley2401, 13 Thorlabs LDC8010 and 2 TECMA 72–2535. Starting from the outer perimeter, the TBU characterization process consisted in injecting optical power into one of the ports of the TBU and sweeping the electrical current bias applied to one of the two heaters. This process was carried out for the 76 thermal tuners present on each of the 2 characterized PCBs. Together with resistance and output optical power, we obtained as a result the normalized coupling constant calibration curves of each TBU. Through this method, we also extracted the phase shift induced by each heater. For inner TBU characterization, we biased outer TBUs to set them in a proper state to access the inner devices. The average loss of each TBU is 0.59 ± 0.10 dB.

The chip can be programmed to operate as a traditional multifunctional single or double input/output signal processor and its operation including the implementation of simple and complex finite (FIR) and infinite impulse response (IIR) filters has been reported in.[19] Most of these operations involve single or cascade optical ring resonators (ORRs) and/or MZI devices that can be independently tuned. A full description regarding the chip fabrication and its optical and electrical characterization in general terms (i. e. regardless of their application as signal processors or multiport interferometers), including the optical losses due to different factors can also be found in.[19]

5. Experiments

We programmed the TBUs of the hexagonal waveguide mesh chip with the suitable injection currents to implement several versions of rectangular universal multiport interferometers.[12]

The 7-cell hexagonal waveguide mesh can implement arbitrary 2×2, 3×3 and 4×4 unitary matrices with complex coefficients For example, **Figure 8** shows the results obtained for simple 2×2 transformations involving complex valued coefficients.[20] The phase shifts are implemented by one or two TBUs marked as PS and shown in the figure. The required phase shift value is obtained by means of an interferometric adjustment technique (see Supporting material). **Table 1** provides the required values for the coupling constants and phases of the MZIs used in these implementations. These are translated into the required injected currents to the phase shifters according to the calibration curves obtained in the chip characterization. The thermal tuner efficiency is 110 ± 15 mW/π, is in fact quite low and is the consequence of using considerably wide (10 um) and long (460 um) heaters in order to prevent the effect of fabrication errors and misalignments. State-of-the-art thermal tuners in Silicon technology can enable much shorter and narrower heaters (around 60 μm and 1 μm, respectively) and, therefore, a considerable improvement in their efficiency. We have normalized the traces to a straight waveguide. An error from the desired response is obtained produced mainly by the variation of the coupling efficiency. For each case, the worst measured error is: 0.48, 0.18 and 0.30 dB.

Figure 9 shows the results obtained of four 3×3 transformations (Identity, Three-way beamsplitter, Discrete Fourier

**ADVANCED
SCIENCE NEWS**

www.advancedsciencenews.com
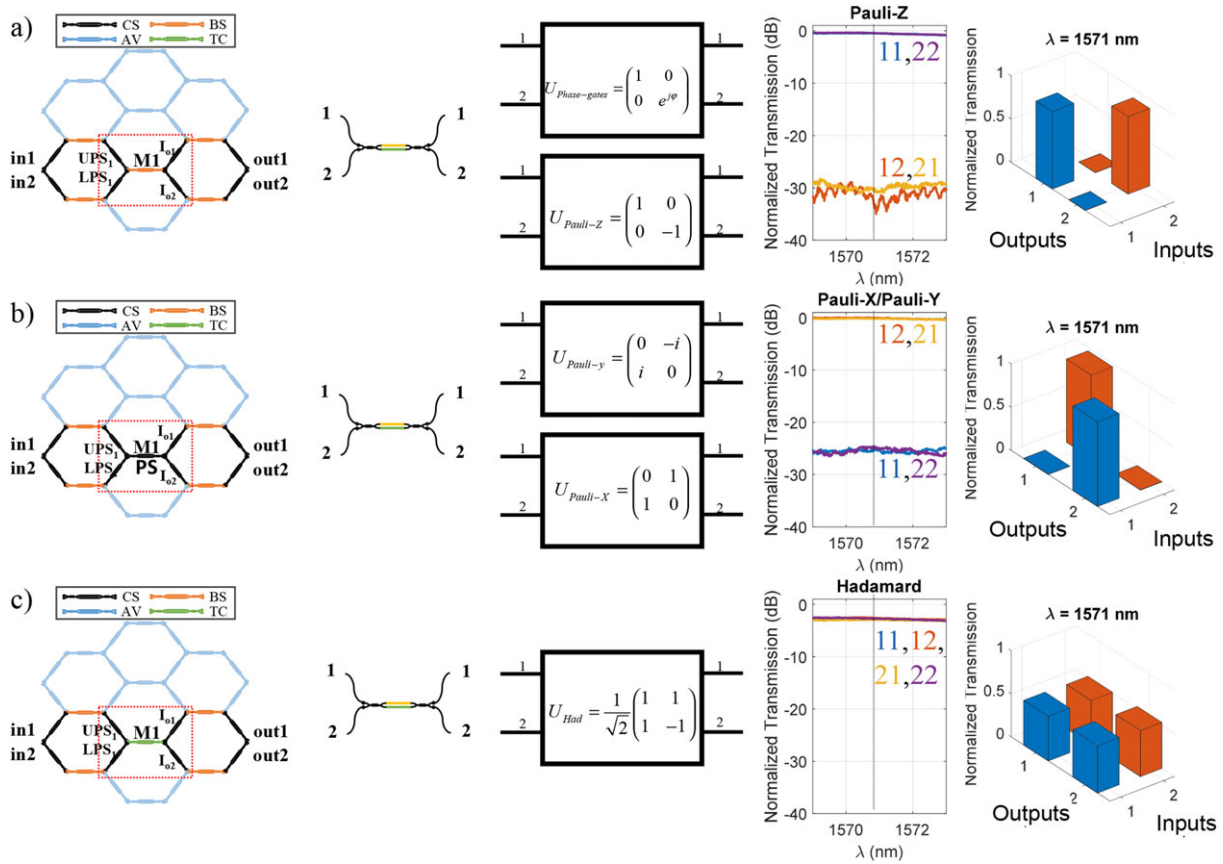
LASER
& PHOTONICS
REVIEWS

www.lpr-journal.org

Figure 8. Experimental results for simple 2 × 2 unitary transformations involving complex-valued matrix coefficients using the hexagonal waveguide mesh. a) Pauli-Z transformation, b) Pauli X and Pauli Y transformations, c) Hadamard transformations. Column 1: 7-cell configuration (CS = MZI in cross state, BS = MZI in bar state, TC = MZI in tunable coupler state, AV = MZI not employed, PS = Phase shifter), Column 2: circuit layout of the implemented interferometer, Column 3: Spectral measurement of all input/output port connections. Column 4: Normalized Bar diagram of the resulting measured unitary matrix for λ = 1571 nm.

Table 1. Required values for the coupling constants and phases of the MZIs used in the hexagonal waveguide mesh configuration of a 2 × 2 interferometers. P indicates that the TBU remains unbiased.

	(a) P–Z		b1) P–X		b2) P–Y		(c) Had	
TBU	k	ϕ	k	ϕ	k	ϕ	k	ϕ
M1	0	0	1	0	1	0	0.5	0
UPS	1	0	1	$-\pi/2$	1	$-\pi$	1	0
LPS	1	0	1	0	1	0	1	0
Io$_1$	1	$\pi/2$	1	0	1	$\pi/2$	1	$\pi/2$
Io$_2$	1	$\pi/2$	1	$-\pi/2$	1	$-\pi/2$	1	$\pi/2$
CS-interconn.	1	0	1	0	1	0	1	0
BS-Type A interconn.	0	$-\pi/2$	0	$-\pi/2$	0	$-\pi/2$	0	$-\pi/2$
BS-TypeB interconn.	0	$\pi/2$	0	$\pi/2$	0	$\pi/2$	0	$\pi/2$
Rest	P	0	P	0	P	0	P	0

Transform (DFT) and a permutation matrix). As with the previous cases, an excellent agreement is obtained between the theoretical and measured matrix coefficients with extinction ratios above 25 dB for the targeted 1 and 0 coefficients. The corresponding coupling and phase values are included in the Supporting Material. For these cases, the worst measured error is 0.22, 0.52 and 1.10 dB.

We finally present the measured results corresponding to the implementation of rectangular 4 × 4 interferometers. **Figure 10** shows the results obtained for three different unitary transformations[20] that support well know operations in quantum information (identity, C-NOT and swap). As with the former cases, an excellent agreement is obtained between the theoretical and measured matrix coefficients with extinction ratios above 25 dB for the targeted 1 and 0 coefficients. **Table 2** provides the required values for the coupling constants and phases of the MZIs used in these implementations. Again, these are translated into the required injected currents to the phase shifters according to the calibration curves obtained in the chip characterization. Note that due to the number of TBUs of the fabricated PIC, this device will be limited to interferometric structures where MB coupling constant setting is equal to 1 (Bar State) for 4 × 4 transformations. For these cases, the worst measured error is 0.60, 1.02 and 0.80 dB.

The bandwidth of the circuits demonstrated in this section is limited by an operation bandwidth of 21 ± 2 nm (–1 dB) and 35 ± 2 nm (–3 dB). This limitation comes from the grating coupler bandwidth employed for the optical input and output ports.
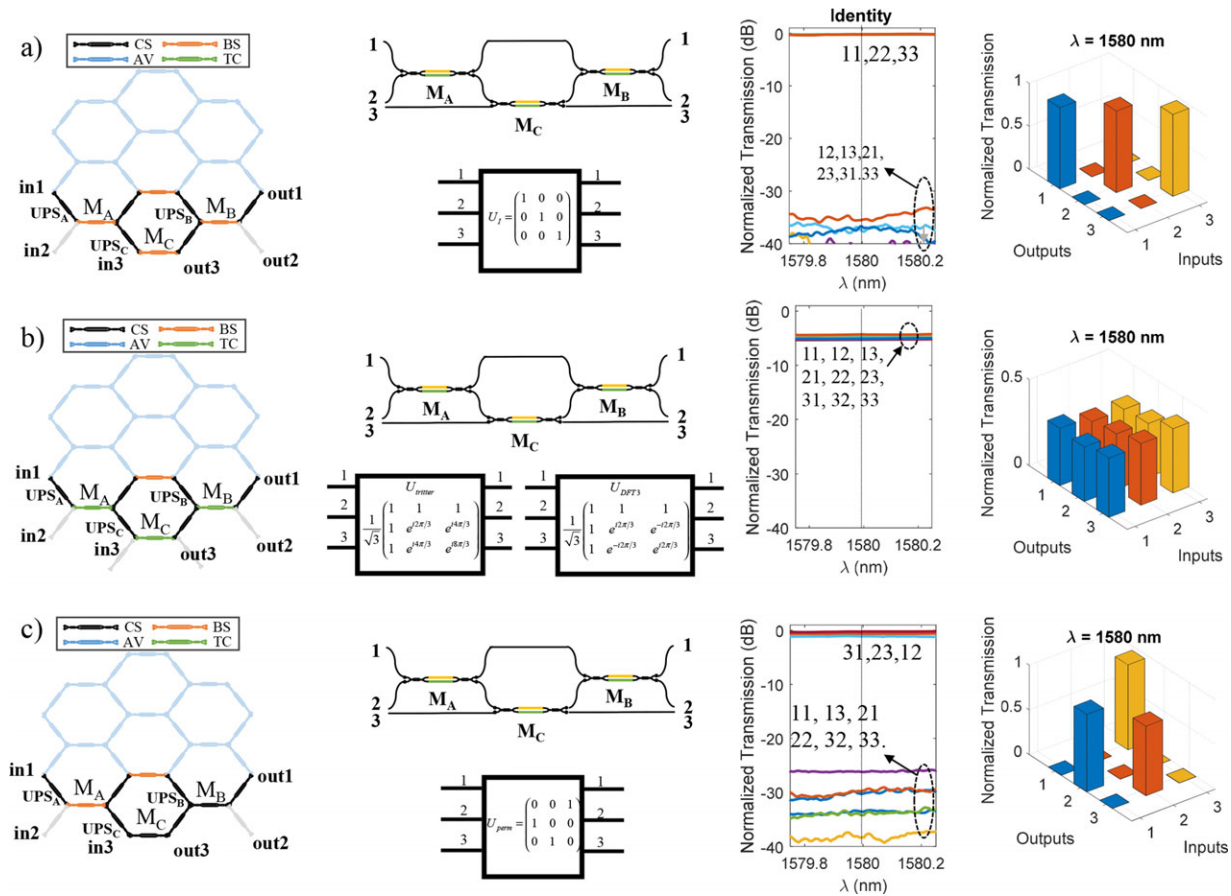
**ADVANCED
SCIENCE NEWS**

www.advancedsciencenews.com

LASER
& PHOTONICS
REVIEWS

www.lpr-journal.org

Figure 9. Experimental results for simple 3 × 3 unitary transformations involving complex-valued matrix coefficients using the hexagonal waveguide mesh. a) Identity transformation, b) Three-way beamsplitter and Discrete Fourier Transform, c) Transformation between input/output channels 1/2, 2/3 and 3/1. Column1: 7-cell configuration (CS = MZI in cross state, BS = MZI in bar state, TC = MZI in tunable coupler state, AV = MZI not employed, PS = Phase shifter), Column 2: circuit layout of the implemented interferometer, Column 3: Spectral measurement of all input/output port connections. Column 4: Normalized Bar diagram of the resulting measured unitary matrix for λ = 1580 nm.

The MMI bandwidth was greater than the vertical couplers bandwidth.

6. Discussion, Summary and Conclusions

Our experimental results have shown the potential of the hexagonal waveguide mesh for implementing 2 × 2, 3 × 3 and 4 × 4 linear optic real and complex-valued unitary transformations. It is important to outline that the value of the proposed waveguide mesh resides in the fact that the same hardware architecture can support either a triangular or a rectangular arrangement for multiport interferometers. In addition, full matrix reconfiguration is achieved by translating the values of the coupling constants and phase shifters (obtained by means of the synthesis algorithms adapted to this architecture) into proper injection currents to the tuning elements according to calibration curves. In this respect, this configuration can help to reduce fabrication costs as the same layout is fabricated regardless the targeted transformation.

An important question that needs to be addressed is related to the structure scalability. Although 2 × 2, 3 × 3 and 4 × 4 interfer-

ometers support by themselves an important number of transformations, in practice, a higher number of input/output ports could be requested to construct more complex circuits.[21–23] In the structure reported in this paper, the number of cells in the chip limits the maximum number of ports. Actually, the mesh scalability is directly related to the number of cells, the number of TBUs and the BULs. For universal interferometers, reducing the BUL brings a trade-off.

For shorter BUL, the propagation losses per TBU will be reduced whereas the crosstalk related to the tuning mechanism (thermal-crosstalk in this work), may increase since it is proportional to the proximity between TBUs. This effect can be mitigated with deeper isolation trenches that the ones employed or by designing an optimum thermal management in the packaging stage. State-of-the-art 3-dB couplers in silicon have insertion losses around 0.15 ± 0.10 dB, so the losses due to these 2 cascade couplers will dominate over state-of-the-art propagation losses, which are around 1 dB/cm.[24]

For larger hexagonal waveguide meshes featuring more cells than those actually required for a certain operation, it will be necessary to program access paths to access the rectangular arrangement, leading to additional balanced losses for all the channels.
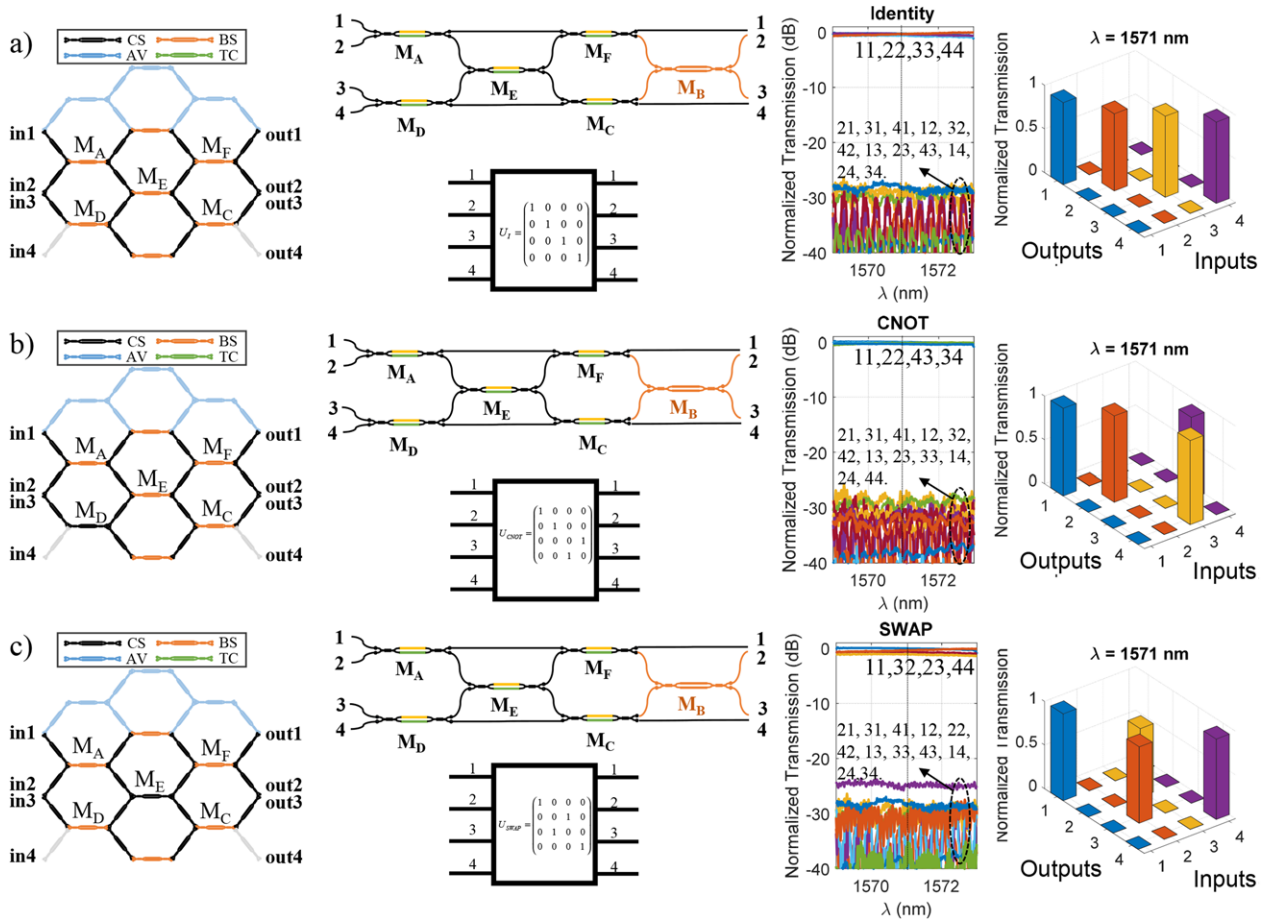
**ADVANCED
SCIENCE NEWS**

www.advancedsciencenews.com

LASER
& PHOTONICS
REVIEWS

www.lpr-journal.org

Figure 10. Configuration of a 4 × 4 interferometer based on a rectangular arrangement. a) Identity transformation, b) C-NOT transformation, c) SWAP transformation. Column1: 7-cell configuration (CS = MZI in cross state, BS = MZI in bar state, TC = MZI in tunable coupler state, AV = MZI not employed), Column 2: circuit layout of the implemented interferometer, Column 3: Spectral measurement of all input/output port connections. Column 4: Normalized Bar diagram of the resulting unitary matrix for λ = 1571 nm.

In contrast, the unused TBUs will be left as redundant components that can be employed in case of failure over a certain chip area, leading to a more robust device.

The bandwidth limitation can be overcome with an optimized design of the vertical couplers or by employing edge-coupling. For example, vertical couplers with a 1–dB bandwidth of 37 nm have been successfully demonstrated in silicon on insulator.[31]

A key advantage of this hexagonal mesh is the possibility to flexibly combine universal interferometers with other classic photonic integrated circuit structures that can be programmed over the mesh as well, such as Mach-Zehnder Interferometers or interferometric cavities.[17,19,25–30] This comes at the expense of more beamsplitters for a certain NxN transformation, that will increase from the minimum N(N-1)/2 figure required for ad-hoc rectangular arrangements, to (3N(N-1)/2)+2N.

The non-ideal performance of the TBUs might include drift during operation. Self-configuring algorithms and on-chip monitoring would provide a more robust dynamic operation. However, we must note that an optical ring resonator was previously programmed in this chip architecture providing a notch wavelength drift of less than 7 pm during 45 min, demonstrating a remarkable robust and stable operation.[19]

The number of cells for a particular design will depend on the size of the targeted circuits to be synthetized/programmed. In practice, the number of electrical DC Pads and its associated control system might limit the number of available TBUs present on the circuit. **Figure 11** plots the number of required electrical ports versus the number of cells. For the reported device, we employed 120 single-point (ground) pads for the electrical control of 60 phase shifters. Out of the chip, some of them were connected to a common ground. Having a common ground port on the circuit can reduce the amount of electrical ports by a factor of 2. The main drawback would then be the appearance of electrical noise, which can be pre-characterized considering the differential resistance of each path. On-chip electronic-photonic integration would relax the space limitations of the internal wirebonding approach. In this sense, different approaches like employing different metal layer levels for the electronic signal routing and flip-chip bonding, through silicon via (TSV) and through oxide via (TOV), have been demonstrated in the last decade and are actually rapidly maturing.[32]

Table 2. Required values for the coupling constants and phases of the MZIs used in the hexagonal waveguide mesh configuration of a tunable 4×4 interferometer based on a rectangular arrangement: P indicates that the TBU remains unbiased.

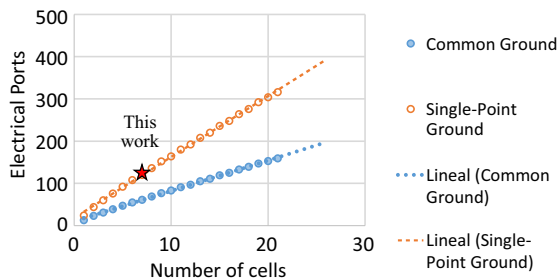|	Identity		C-NOT		SWAP	
TBU	k	ϕ	k	ϕ	k	ϕ
M_A	0	0	0	0	0	0
A-UPS	1	$-\pi$	1	$-\pi$	1	$-\pi$
M_B	0	0	0	0	0	0
B-UPS	N1	0	1	0	1	0
M_C	0	0	0	0	0	0
C-UPS	1	0	1	0	1	0
M_D	0	0	1	0	0	0
D-UPS	1	$-\pi$	1	$-\pi$	1	$-\pi$
M_E	0	0	0	0	1	0
E-UPS	1	0	1	$-\pi$	1	0
M_F	0	0	0	0	0	0
F-UPS	1	$-\pi$	1	0	1	$-\pi$
A,B,C,D, E,F-LPS	1	0	1	0	1	0
Io_1	1	$-\pi/2$	1	$\pi/2$	1	$-\pi/2$
Io_2	1	$-\pi/2$	1	$\pi/2$	1	$-\pi/2$
Io_3	1	$\pi/2$	1	$-\pi/2$	1	$-\pi/2$
Io_4	1	$-\pi/2$	1	$-\pi/2$	1	$-\pi/2$
CS-interconn.	1	0	1	0	1	0
BS-Typ. A interconn.	0	$-\pi/2$	0	$-\pi/2$	0	$-\pi/2$
BS-Typ. B interconn.	0	$\pi/2$	0	$\pi/2$	0	$\pi/2$
Rest	P	0	P	0	P	0

Figure 11. Electrical ports vs number of cells for 2 different ground configurations.

Supporting Information

Supporting Information is available from the Wiley Online Library or from the author.

Acknowledgements

Conflict of Interest

The authors have declared no conflict of interest.

Keywords

[1] M. Reck, A. Zeilinger, H. J. Bernstein, P. Bertani, *Phys. Rev. Lett.* **1994**, *73*, 58.

[2] D. A. B. Miller, *Photon. Res.* **2013**, *1*, 1.

[3] J. Carolan, C. Harrold, C. Sparrow, E. Martin-López, N. J. Russell, J. W. Silverstone, P. J. Shadbolt, N. Matsuda, M. Oguma, M. Itoh, G. D.Marshall, M. G. Thompson, J. C. F. Matthews, T. Hashimoto, J. L. O'Brien, A. Laing, *Science* **2015**, *349*, 711.

[4] J. W. Silverstone, D. Bonneau, J. L. O'Brien, M. G. Thompson, *IEEE J. Sel. Top. Quantum Electron.* **2016**, *22*, 390.

[5] B. J. Metcalf, N. Thomas-Peter, J. B. Spring, D. Kundys, M. A. Broome, P. C. Humphreys, X.-M. Jin, M. Barbieri, W. S. Kolthammer, J. C. Gates, B. J. Smith, N. K. Langford, P. G. R. Smith, I. A. Walmsley, *Nat. Commun.* **2013**, *4*, 1356.

[6] J. Capmany, I. Gasulla, D. Perez, *Nat. Photonics* **2016**, *10*, 6.

[7] D. A.B. Miller, *Opt. Express* **2013**, *21*, 6360.

[8] F. Morichetti, A. Annoni, S. Grillanda, N. Peserico, M. Carminati, P.Ciccarella, G. Ferrari, E. Guglielmi, M. Sorel, A. Melloni, in *Optical Fiber Communication Conference* (**2016**), paper ThE3.7.

[9] L.-N. Chen, E. Hall, L. Theogarajan, J. Bowers, *IEEE Photon. J.* **2011**, *3*, 834.

[10] R. Stabile, A. Albores-Mejia, A. Rohit, K. A. Williams, *Microsyst. Nanoeng.* **2016**, *2*, 15042.

[11] D. A. B. Miller, *Optica* **2015**, *2*, 747.

[12] W.R. Clements, P.C. Humphreys, B.J. Metcalf, W.S. Kolthammer, I.A. Walmsley, *Optica* **2016**, *3*, 1460.

[13] S. Grillanda, M. Carminati, F. Morichetti, P. Ciccarella, A. Annoni, G. Ferrari, M. Strain, M. Sorel, M. Sampietro, A. Melloni, *Optica* **2014**, *1*, 129.

[14] A. Ribeiro, A. Ruocco, L. Vanacker, W. Bogaerts, *Optica* **2016**, *3*, 1348.

[15] *Nat. Photonics* **2016**, *10*, 1. Editorial.

[16] L. Zhuang, C. G. H. Roeloffzen, M. Hoekman, K-J. Boller, A. J. Lowery, *Optica* **2015**, *2*, 854.

[17] D. Pérez, I. Gasulla, J. Capmany, R. A. Soref, *Opt. Express* **2016**, *24*, 12093.

[18] D.A.B. Miller, *Opt. Express* **2012**, *20*, 23985.

[19] D. Perez, I. Gasulla, L. Crudgington, D. J. Thomson, A. Khokhar, K. Li, W. Cao, G. Z. Mashanovich, J. Capmany, *Nat. Commun.* **2017**, *8*, 636.

[20] M.A. Nielsen, I.L. Chuang, *Quantum Computation and Quantum Information*, Cambridge University Press **2001**.

[21] A. Peruzzo, A. Laing, A. Politi, T. Rudolph, J. L. O'Brien, *Nat. Commun.* **2011**, *2*, 224.

[22] N. Spagnolo, C. Vitelli, M. Bentivegna, D. J. Brod, A. Crespi, F. Flamini, S. Giacomini, G. Milani, R. Ramponi, P. Mataloni, R. Osellame, E. F. Galvão, F. Sciarrino, *Nat. Photonics* **2014**, *8*, 615.

**ADVANCED
SCIENCE NEWS**

www.advancedsciencenews.com

LASER
&PHOTONICS
REVIEWS

www.lpr-journal.org

[23] D. Bonneau, E. Engin, K. Ohira, N. Suzuki, H. Yoshida, N. Iizuka, M. Ezaki, C. M. Natarajan, M. G. Tanner, R. H. Hadfield, S. N. Dorenbos, V. Zwiller, J. L. O'Brien, M. G. Thompson, *New J. Phys.* **2012**, *14*, 045003.

[24] L. Chrostowski, M. Hochberg, Silicon Photonics Design: *From Devices to Systems*. Cambridge University Press **2015**.

[25] C.K Madsen, J.H. Zhao, *Optical Filter Design and Analysis: A Signal Processing Approach*. Wiley **1999**.

[26] K. Jinguji, *J. Lightw. Technol.* **1995**, *13*, 73.

[27] K. Jinguji, *J. Lightw. Technol.* **1996**, *14*, 1882.

[28] C.K Madsen, *J. Lightw. Technol.* **2000**, *18*, 860.

[29] A. Yariv, Y. Xu, R. K. Lee, A. Schere, *Opt. Lett.* **1999**, *24*, 711.

[30] J. E. Heebner, P. Chak, S. Pereira, J. E. Sipe, R. W. Boyd, *J. Opt. Soc. Am. B* **2004**, *21*, 1665.

[31] L. Liu, M. Pu, K. Yvind, J. M. Hvam, *Appl. Phys. Lett.* **2010**, *96*, 051126.

[32] N. DiLello Heidel, N. G. Usechak, C. L. Dohrman, J. A. Conway, *IEEE J. Sel. Top. Quantum Electron.* **2016**, *22*, 8300209.

1700219 (13 of 13)